Retracing the decaying swell across the Pacific with CFOSAT SWIM data

Xiaoyu Sun[1], Jian Sun[1], Wenqing Zhang[2], and Qingxiang Liu[3]

[1]Ocean University of China
[2]College of Oceanic and Atmospheric Sciences, Ocean University of China
[3]University of Melbourne

November 22, 2022

Abstract

Oceanic swells generated by storms can sometimes propagate over long distances across the oceans. In this study, we propose a new method to retrace the sources and routes of swells generated in the Southern Ocean using the Surface Waves Investigation and Monitoring (SWIM) instrument onboard the Chinese-French Oceanography Satellite (CFOSAT), ERA5 reanalysis data, and buoy data from the National Data Buoy Center (NDBC). We found 25 routes for swells that were generated by 4 ocean storms in the Southern Ocean from May to August 2019. The decay rate of the swell energy is found to increase with the spectral width of the initial swell field. The general rate of increase of the peak wavelength is ~0.01 m/km, and is apparently dependent on the spectral width. We used a point source model and the wave model data from a two-month run of WAVEWATCH III (WW3) to calculate the linear dissipation rates of swells propagating at different stages. The linear dissipation rate decreases with increasing distance from the swell source. The point source model yielded dissipation rates of -1.4 to 2.4×10^{-7} m^{-1}. In addition, nonlinear dissipation rates were calculated based on the air–sea interaction theory and wave–turbulence interaction theory.

Hosted file

`essoar.10510664.1.docx` available at https://authorea.com/users/535335/articles/598730-retracing-the-decaying-swell-across-the-pacific-with-cfosat-swim-data

Xiaoyu Sun[1], Jian Sun[1,2], Wenqing Zhang[1,2], Qingxiang Liu[1,2]

[1]College of Oceanic and Atmospheric Sciences, Ocean University of China, Qingdao, China.

[2]Physical Oceanography Laboratory/CIMST, Ocean University of China and Qingdao National Laboratory for Marine Science and Technology, Qingdao, China.

Corresponding author: Wenqing Zhang (wqzhang@ouc.edu.cn)

Key Points:

- A new method of backtracking the Pacific swell routes is proposed.

- The spectral width is used as an indicator of the degree of influence of spherical spreading on swell energy decay.

- The wave model data which ignores swell dissipation and negative wind input is used to calculate the dissipation rates from swell sources.

Abstract

Oceanic swells generated by storms can sometimes propagate over long distances across the oceans. In this study, we propose a new method to retrace the sources and routes of swells generated in the Southern Ocean using the Surface Waves Investigation and Monitoring (SWIM) instrument onboard the Chinese-French Oceanography Satellite (CFOSAT), ERA5 reanalysis data, and buoy data from the National Data Buoy Center (NDBC). We found 25 routes for swells that were generated by 4 ocean storms in the Southern Ocean from May to August 2019. The decay rate of the swell energy is found to increase with the spectral width of the initial swell field. The general rate of increase of the peak wavelength is ~0.01 m/km, and is apparently dependent on the spectral width. We used a point source model and the wave model data from a two-month run of WAVEWATCH III (WW3) to calculate the linear dissipation rates of swells propagating at different stages. The linear dissipation rate decreases with increasing distance from the swell source. The point source model yielded dissipation rates of -1.4 to 2.4×10^{-7} m^{-1}. In addition, nonlinear dissipation rates were calculated based on the air–sea interaction theory and wave–turbulence interaction theory.

Plain Language Summary

Transoceanic swells can carry energy away from the storm center after being generated. Swells reaching the shallow ocean area can affect the safety of the offshore and nearshore facilities and projects. Due to the lack of observational data, the mechanisms of swell propagation and decay have always been regarded as difficult points in wave forecasting. In this study, we used the observational data from the satellite and buoys with the wave model data to retrace the swell routes in the Pacific. We then analyzed the evolution of wave parameters during propagation and calculated the dissipation rates of different stages of swell routes.

1. Introduction

Swells are either wave components that originate in other ocean areas, or are generated locally but no longer absorb energy from local winds after the wind weakens or changes its direction. Compared with wind waves, swell typically has a longer wavelength and a more regular wave form. Swells generated in the storms of the westerlies provide one of the most persistent components of the global wave climate (Alves, 2006). The climatology of the global wave field shows that global surface waves are strongly dominated by swells, and this is because swells have predominantly high energy weight and occurrence probability, especially in the tropical oceans (Chen et al., 2002; Semedo et al., 2011; Zheng et al., 2016). Swells play an important role with respect to air–sea interaction processes and momentum flux. By interacting with air flows, swells change the original wind profile in the marine atmospheric boundary layer, and thus alter the sea surface roughness and drag coefficient (Badulin & Zakharov, 2017; Drennan et al., 1999; Hwang, 2008; Kudryavtsev & Makin, 2004). The study of swells is also beneficial for the planning of shipping routes and the protection of offshore and coastal facilities. Swells can be dangerous for vessels and offshore platforms because the co-occurrence of wind waves and swell leads to a higher possibility of accidents, even during in low sea states (Zhang & Li, 2017). The hydrodynamic phenomena caused by swells generated by a distant storm may result in flooding in coastal areas (Andrade et al., 2013). Currently, the calculation of wave models still needs improvement, especially in the swell decay term. The mechanisms that drive swell propagation and attenuation remain unclear because of the limited amount of data available, and this gap in our knowledge leads to errors in ocean modelling.

About half a century ago, researchers using in situ measurements from the Pacific discovered that swells can cross the entire ocean from their source (Munk et al., 1963; Snodgrass et al., 1966). These pioneering works provided a basic understanding of the propagation of swells, and further studies improved our knowledge of this process. Hamilton (1992) compared the data related to wave periods from several buoys near the eastern coast of North America and approximately located the source of swell in the ocean field near the Antarctic by examining weather maps. However, when using this method, no wave direction data were collected, and no intermediate points along the route of the swells could be used for verification. Remya et al. (2016) considered the relationship between high swell events along the coast of the northern Indian Ocean and low-pressure systems in the southern Indian Ocean, and Zheng et al. (2018) reported that swells take 2–6 days to cross the Indian Ocean from south to north. Wang et al. (2016) identified convergence regions for storm-induced swells using a backtracking method and found good correspondence between the distribution of these regions and ocean storms. Using a 10-year dataset obtained with the synthetic aperture radar (SAR), Li (2016) reconstructed the propagation routes of swells and the distribution of swell pools in the global oceans.

Swells can propagate over long distances because they decay very slowly, posing

difficulties to quantify the physical processes contributing to the decay. Snodgrass et al. (1966) calculated the rate of decay using data from stations set along the great circle from New Zealand to Alaska, and found that the dissipation rate of swells with wave periods of less than 13 s was 2×10^{-7} m^{-1}. This was the first time researchers had calculated the swell decay rate, but the influence of island-sheltering led to significant errors in their calculations. Using the L2 product of SAR, Collard et al. (2009) proposed a new method of tracking the routes of swells along great circles around the Earth, and obtained a dissipation rate of 3.7×10^{-7} m^{-1} for swells with a period of 15 s. Based on these results, Ardhuin et al. (2009) proposed that swell decay is related to the loss of momentum caused by air–sea friction. Later, based on laboratory tests, Babanin (2012) attributed the attenuation of swells to turbulence produced by orbital motion or those fed from the swell orbital energy. Young et al. (2013) used an altimetric database that included significant wave height (SWH) and wind speed measurements, together with model data, and found a dissipation rate around 7×10^{-7} m^{-1}.

Satellite remote sensing has expanded the amount of data available for research into swell propagation and decay, but this is still insufficient. To date, many studies have been based on SAR data because SAR is the only instrument carried by a satellite that can provide data related to wave spectra and directions. However, the process of retrieving wave spectra from the original data collected by SAR is complicated by the nonlinear nature of the relationship between the SAR image and the ocean surface elevation (Krogstad, 1992).

The Chinese-French Oceanography Satellite (CFOSAT) was launched jointly by China and France in 2018. The Surface Waves Investigation and Monitoring (SWIM) instrument onboard the CFOSAT is a real-aperture radar that can also collect data related to wave spectra and other wave parameters. Moreover, the inversion used to obtain the wave spectra from the original SWIM data is simpler than that required for SAR images. This new monitoring instrument is providing high-quality data that has expanded our opportunities to study swells.

Our aim here is to use the CFOSAT SWIM data to investigate the decay of swells as they cross the Pacific. The remainder of the paper is organized as follows. Section 2 introduces the data from the SWIM, National Data Buoy Center (NDBC) buoys, ERA5, and WAVEWATCH III (WW3) hindcast. Section 3 describes the methodology of retracing; in Section 4 we analyze the influence of spherical spreading and energy dissipation. Finally, our conclusions are summarized in Section 5.

1. Data Sources

We used SWIM data and ERA5 reanalysis data to retrace the paths and sources of the swells. Data from the NDBC buoys located near the western coast of North America were used to determine the arrival times of swells from the southwest Pacific.

1. CFOSAT SWIM

CFOSAT was launched in 2018 to measure sea surface wind and waves. The satellite travels along a sun-synchronous orbit and has a large detection range covering the area between 83°N and 83°S; its revisit cycle is 13 days. The near-real-time (NRT) and the L2 data used in this paper were obtained from the wave scatterometer SWIM, a Ku band real-aperture radar with an antenna aperture size of about $2° \times 2°$. A rotatable antenna and six near-nadir conical scanning beams are the core elements of SWIM and make it possible to obtain omnidirectional wave spectra. Among these beams, the nadir beam can give an accurate value of SWH, while the 6°, 8°, and 10° beams are referred to as the "spectral beams" because the directional ocean wave spectra could be determined using measurements from these three beams (Hauser et al., 2021).

The NRT data are the along-track data and are processed within 3 hours of acquisition. This dataset includes information regarding wave parameters (SWH, peak wavelength, and peak direction) and the directional ocean wave spectra. The spectra are calculated in geographical boxes of about 70×90 km^2, and is partitioned into three main components. To ensure that the wave spectra can describe the wave conditions effectively, only the part of the ocean wave spectra with wave numbers between 0.01 and 0.2 m^{-1} are retained in the data. Furthermore, the direction resolution of the spectra is 15°.

The L2 data (version 5.1.2) were acquired using an updated noise reduction technique. This provided us with more accurate wave spectra, especially in the along-track direction, and we compared the parameters from different partitions of the L2 and NRT data to check if the data are reliable and consistent. Both the NRT data and the L2 data are provided by the Centre National d'Etudes Spatiales (CNES) mission center.

1. NDBC Buoys

Buoy data were obtained from the NDBC (https://www.ndbc.noaa.gov/), using 46047, 46059, 51002, and 51004 buoys located off the western coast of North America. The wave spectra data and the standard meteorological data from buoys are reported hourly, in which the SWH is averaged over a 20-min period and the mean wave direction (MWD) refers to the average wave direction for the dominant wave period (DPD).

1. WAVEWATCH III (WW3)

The wave hindcast dataset that we used to calculate the spherical dispersion of swells is based on runs with the WAVEWATCH III (The WAVEWATCH III Development Group; 2019) and the observation-based source term parameterization (ST6; Zieger et al. 2015, Liu et al. 2019). The simulations are forced by the ERA5 winds and run on an irregular–regular–irregular (IRI) grid system (approximately 25 km; Rogers & Linzell, 2018). The initial state of the wave field was generated using data from April 2019. Two different two-month (May–July 2019) WW3 run were conducted: the first with all of the source

terms considered (Test A), and the second without considering the sink of energy related to negative wind input and swell dissipation (Test B). The reader is referred to Liu et al. (2021) for other model settings.

1. ERA5 Reanalysis

To retrace the source of the swells, we also used ERA5 reanalysis data (https://www.ecmwf.int/en/forecasts/datasets/reanalysis-datasets/era5). ERA5 is an atmospheric reanalysis dataset maintained by the European Centre for Medium-Range Weather Forecasts (ECMWF) and provides hourly data of wave parameters gridded at the global scale with a horizontal resolution of 0.5°×0.5° (Hersbach et al., 2020).

1. Methodology

As mentioned above, the time period covered by all data was May to August 2019, which corresponds to the austral winter months. Intense winds blow over the Southern Ocean and storms become more active during this winter period. As a result, more swells are generated and propagate away from this ocean area. In this paper, we used three steps to retrace the trajectories of the swells, as described below.

Previous studies have reported swells traveling from the Southern Ocean to Alaska (Munk et al., 1963; Snodgrass et al., 1966). We hypothesized that the swells analyzed in the present study would travel by similar routes. Therefore, the first step in our retracing procedure was to find eligible cases of swells that passed over the NDBC buoys located near the western coast of North America. Given that swells usually have a longer period than wind waves, we set a criterion that only waves with periods longer than 19 s would be retained. In addition, because swells have very low dissipation rates, it is difficult to analyze the mechanism of dissipation along a short path. Swells coming from the west are most likely to originate from the westerly belt in the Northern Hemisphere, and their propagation routes are relatively short; consequently, these cases were also discarded. Swells coming from 180° to 225° (clockwise from the north) were retained because they might have originated from the Southern Ocean and far from the buoys.

The NDBC buoy data that met both of the conditions outlined above record the time that the swells arrived at the buoy, and we refer to this time as T_B. However, buoys are fixed and can collect data only from waves near the coast. Therefore, our next step was to use the SWIM data to backtrack the routes of the swells. There is a 180° ambiguity in the wave direction in the SWIM data. To obtain the exact direction of the swell, we compared the ERA5 reanalysis data with the SWIM data at the same place and time. If the difference in the wave direction provided by the two datasets was more than 180°, then we added (or subtracted) 180° to (or from) the direction recorded in the SWIM data.

After this preprocessing, we set the following criteria to select the swell partitions (hereafter P_{SWIM}) from all the SWIM data.

i. The time when the SWIM data were collected should be before T_B.

ii. The wavelength of P_{SWIM} should be in between 0.85-1.03 times the wavelength of the selected NDBC buoy data.

iii. The wave direction of P_{SWIM} should be within 15° of the wave direction of the buoy data.

iv. The group velocity V_g was calculated as follows:

$$V_g = \frac{1}{2}\sqrt{\frac{g\lambda}{2\pi}}, \tag{1}$$

where λ is the wavelength of P_{SWIM}. That is, the theoretical distance of swell propagation is $D_{t_1} = V_g \cdot t$. Note that t is the time spent by the swell partition propagating from the location where it was observed by SWIM to the location of the buoy. We also know the real distance between the two points (D_{r_1}). Therefore, $\Delta D_1 = \left| D_{t_1} - D_{r_1} \right|$, and we require:

$$\Delta D_1 < min[200\ km,\ 5\% \times \min\left(D_{r_1}, D_{t_1}\right)]. \tag{2}$$

v. No land barrier exists between the two points.

We recorded the time of P_{SWIM} as T_S. The last step was to locate the sources using the ERA5 reanalysis data. In this case, the criteria are given as follows.

i. The time of the swell source should be before T_S.

ii. The difference between the source direction and the direction of P_{SWIM} should be less than 15°.

iii. If we connect the location of the source and P_{SWIM}, the difference between the orientation of this great circle and the wave direction of P_{SWIM} should be less than 15°.

iv. We record the difference between the theoretical distance (D_{t_2}) and the real distance (D_{r_2}) between P_{SWIM} and the swell source as ΔD_2, and it should satisfy the following condition:

$$\Delta D_2 < min[200\ km,\ 5\% \times \min\left(D_{r_2}, D_{t_2}\right)]. \tag{3}$$

v. No land barrier exists between the two points.

For all points that satisfied the five conditions defined above, we created figures to check the spatial distribution of their time, mean wave period (MWP), and

SWH. Figure 1 presents 6 of the 25 cases and shows that when the distance between these points and P_{SWIM} decreases, the time difference between them also decreases, and so does the SWH. The change in MWP is relatively small, and typically the MWPs exceed 10 s. To select the swell source among those points, we first considered the location of the maximum SWH, while also considering the continuity of time, and requiring no abrupt variation in MWP.
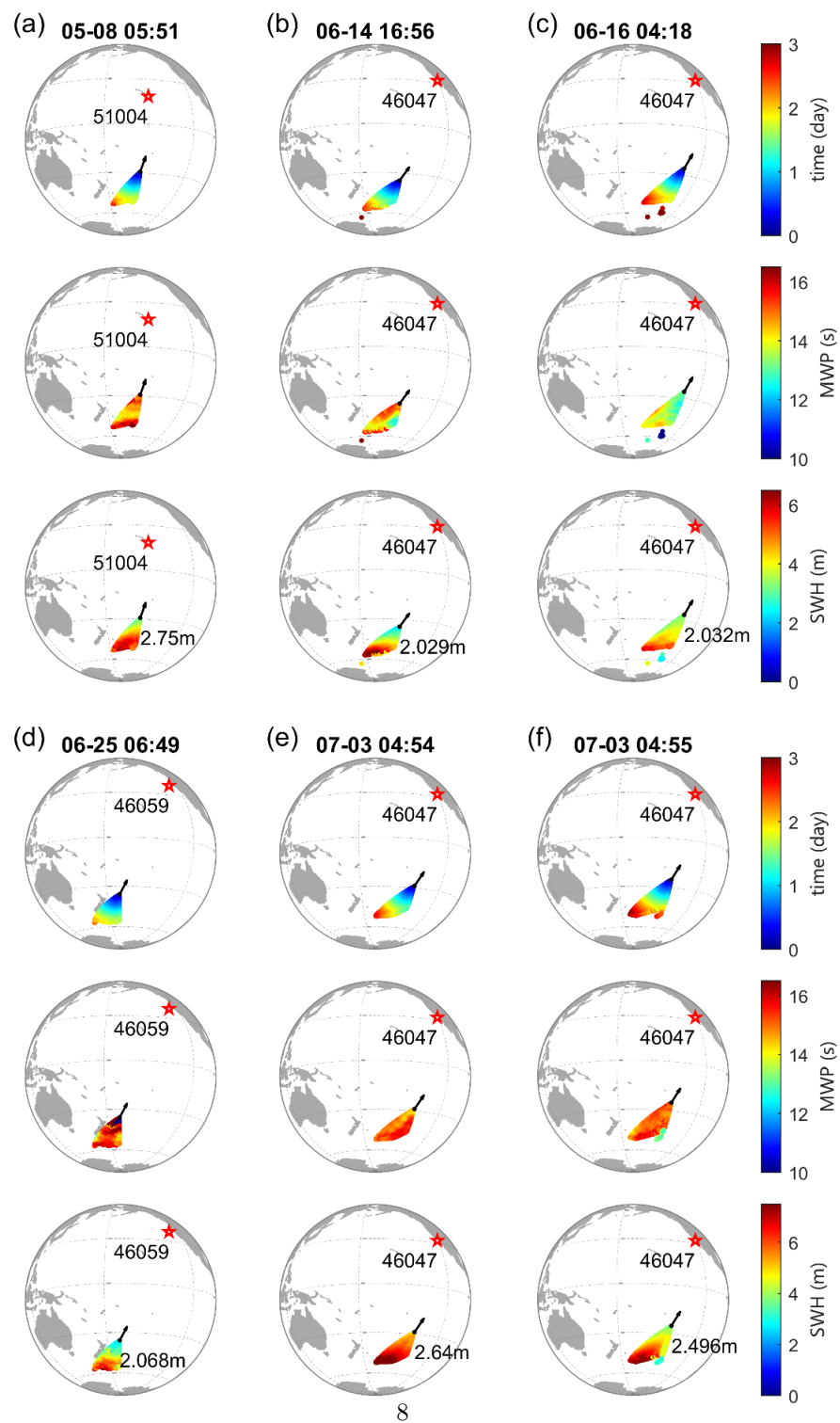
Figure 1. Spatial distribution of MWP, SWH, and the time interval of the WW3 output data points that satisfy the five conditions outlined in Section 3. 'Time' shown in the top plot of each panel refers to the time interval between the data points from WW3 (colored points) and SWIM (location of vector). The vectors show the wave direction of the SWIM data. The numbers near the vectors are the SWH of the SWIM data. The red stars are the locations of the NDBC buoys. (a)–(f) Data from six different swell routes at different times. The dates and times next to the labels (a)–(f) indicate the times of the SWIM data.

Thus far, we have outlined all the steps employed in the retracing process, and the sketch map of swell propagation is shown in Figure 2. In the following sections, we will use points S, C, and B to represent the swell sources, the SWIM data points on the swell routes, and the NDBC buoy data points on the swell routes, respectively. In addition, R1, R2, and R3 indicate the three different parts of the swell routes.
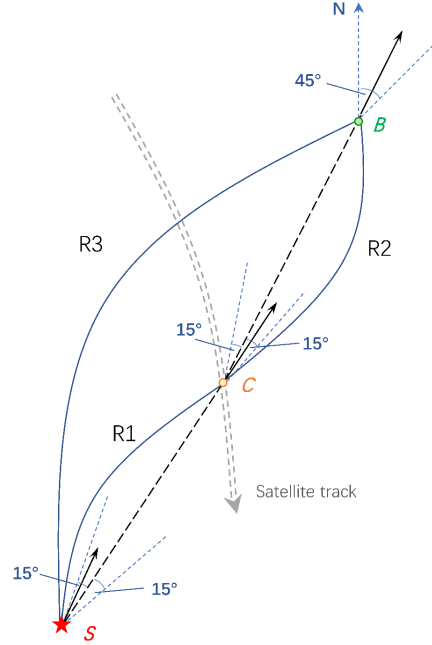
Figure 2. Sketch map of swell propagation. The red star is the location of the swell source, the yellow point is the location on the swell route that was detected by SWIM, and the green point is the location of the NDBC buoy. The black arrows show the direction of the swell at different locations. The black dashed line represents the route of the swell from source to buoy, and the grey dashed line represents the CFOSAT track. The blue dashed lines with angles of 15° and 45°show the direction range used to select the swell data. The blue arcs show the three sections of the swell route, of which R3 represents the entire

route from the storm center to the NDBC buoy.

1. Results

4.1 Routes and sources

We identified 25 swell routes associated with the 4 main storms that occurred during our study period on 5–6 May 2019, 6–14 June 2019, 21 June to 1 July 2019, and 7–8 July 2019, respectively. To ensure that the routes were reliable, we plotted the distribution of the surrounding wave field, as simulated by the WW3, before and after the time of point C (i.e., P_{SWIM}). Figure 3 shows 6 of the 25 cases and we can see that the storms propagate towards the east, and the directions of the swells are generally northeastward. In most cases, the wave parameters shown by the SWIM data are consistent with the wave field data from the WW3 output. The swells for which this was not true were excluded from our analysis. In addition, we excluded the cases when the SWIM version 5.1.2 data that were not consistent with the NRT data. After performing this validation procedure, we identified 21 credible swell routes that were suitable for further analysis.
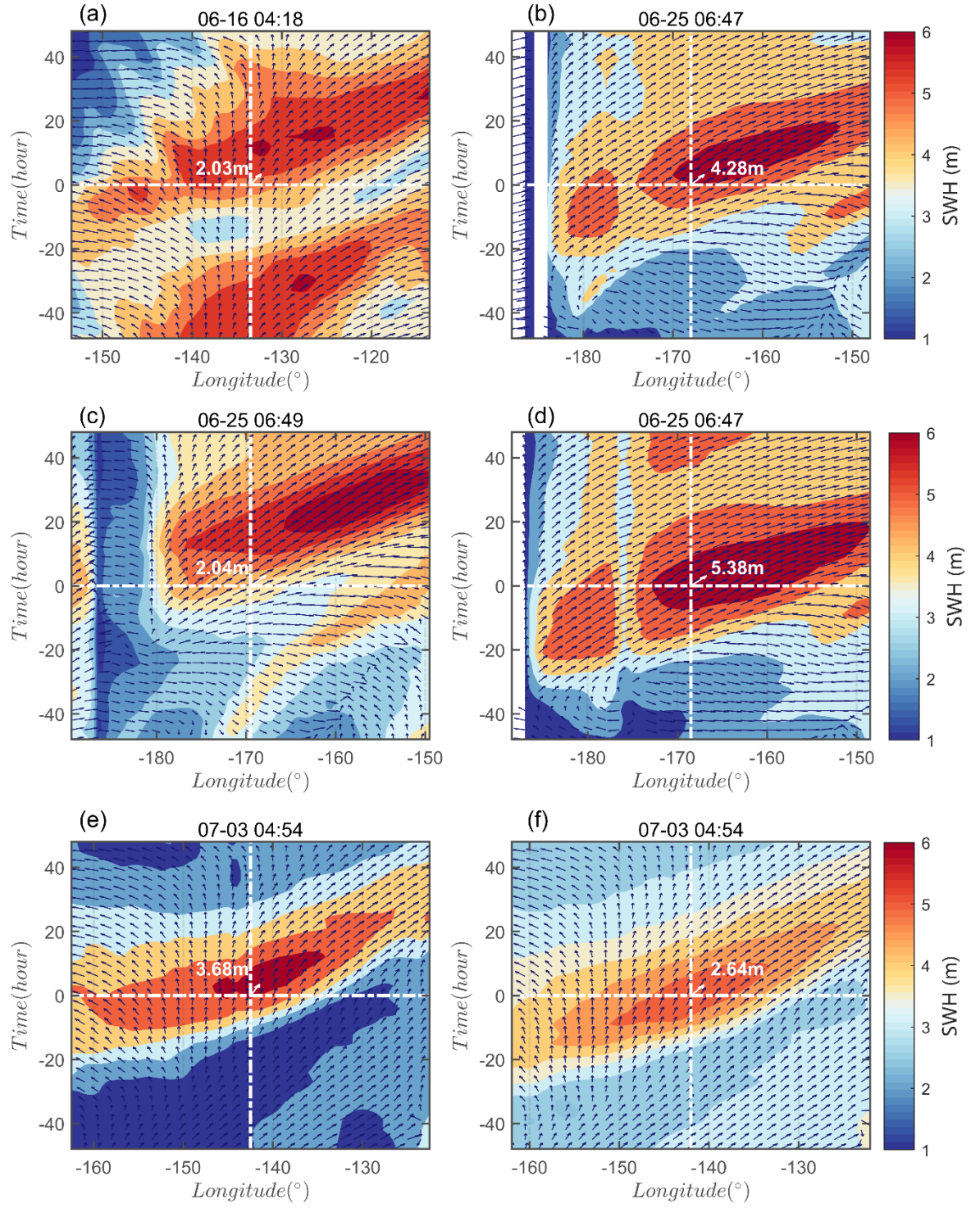
Figure 3. (a)–(f) Distribution of SWH (contours) and wave direction (vectors) with time and longitude. The length of the vectors indicates the wave periods. The white vector in the center of the figure shows the swell partition detected by SWIM. The number near the vector is the SWH of the SWIM data. The panel titles show the collection times of the SWIM data.

Figure 4 shows three swell sources that were related to one of the four storms (the storm from 21 June to 1 July), and this storm propagates towards the east while generating swells. Two sources were found at 9:00 23 June using the retracing procedure, and both were analyzed because it was not clear which of them was the more accurate.
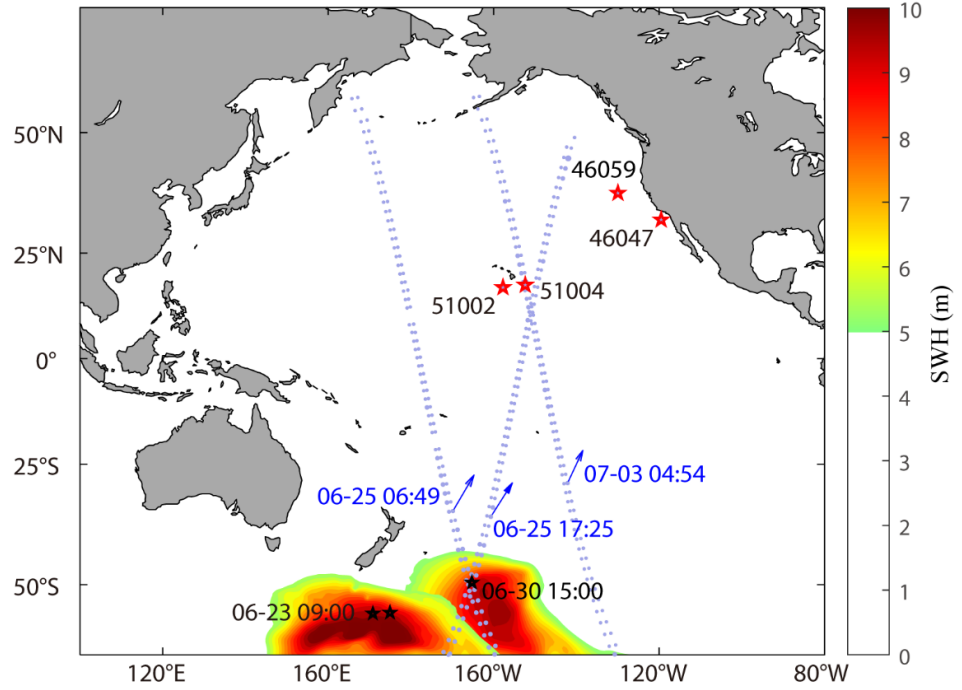
Figure 4. Movement of an ocean storm over time and the swells generated by the storm at different locations. The black stars and numbers show the locations and times of the swell sources, respectively. The red stars show the locations of the four buoys, and the numbers next to the red stars are the names of the buoys. The dotted lines represent the CFOSAT tracks, and the blue arrows are the directions of swells recorded by SWIM at different times (blue numbers).

4.2 Frequency dispersion and angular spreading

According to the linear wave dispersion relationship, when waves are generated

12

in an ocean area, each partition of the wave spectrum travels at a different speed. Components with longer wave periods always travel faster than those with shorter periods. As a result, different components will become separated from each other, and this is referred to as frequency dispersion. Furthermore, a difference in wave directions can lead to the discretization of the

different wave components; i.e., angular spreading. Both of these processes are important factors with respect to swell energy attenuation, and can cause significant changes in wave spectra. To clarify the influence of spherical spreading on swell decay, we compared the one-dimensional wave spectra of swells at points C and B from every swell route. First, we transformed the two-dimensional wave height spectrum $F(k, \varphi)$ obtained from SWIM into a one-dimensional frequency spectrum $S(f)$:

$$\int S(f)\mathrm{df} = 2 \int F(k, \varphi)\mathrm{kdkd} , \quad (4)$$

and compared it with the frequency spectrum calculated using the NDBC buoy data. The frequency of the swell partition is around 0.05 s^{-1} (Figure 5), and both the energy density of the whole spectrum and the swell partition decrease during swell propagation. The two-dimensional swell spectra at points B and C, corresponding to one-dimensional spectra shown in Fig. 5d, are compared in Figure 6, and it is apparent that the swell partitions at the two points are in similar directions; the trend in energy decay is also clear. Other partitions are also evident around the swell partition at point B, and were possibly generated by the local wind.
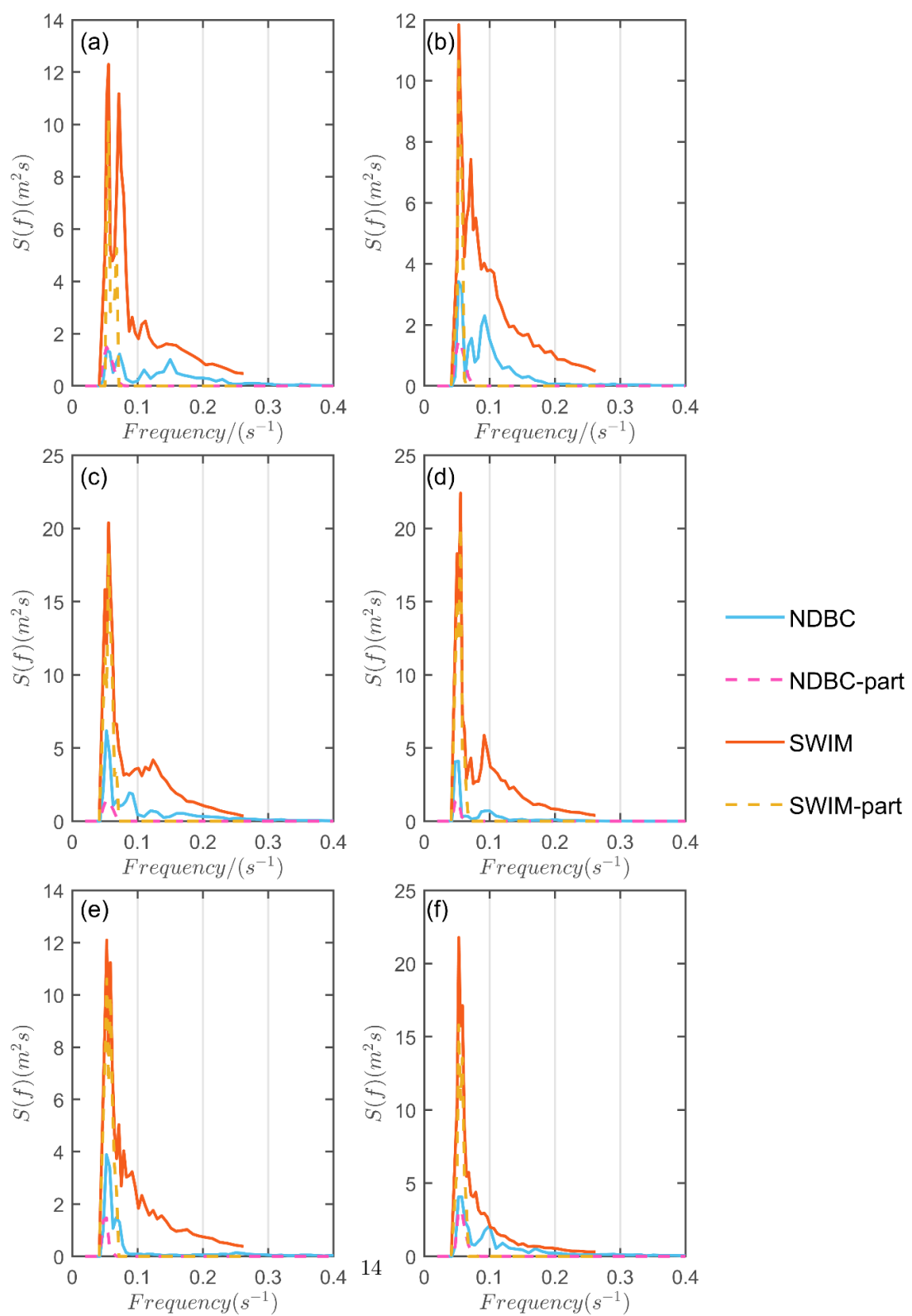
14

Figure 5. Distribution of energy density $S(f)$ with frequency for six routes selected. The dark orange lines represent the energy density of the SWIM data, the blue lines represent the energy density of the NDBC data, the light orange and pink dashed lines represent the energy density of the main swell partition of the SWIM data and NDBC data, respectively.
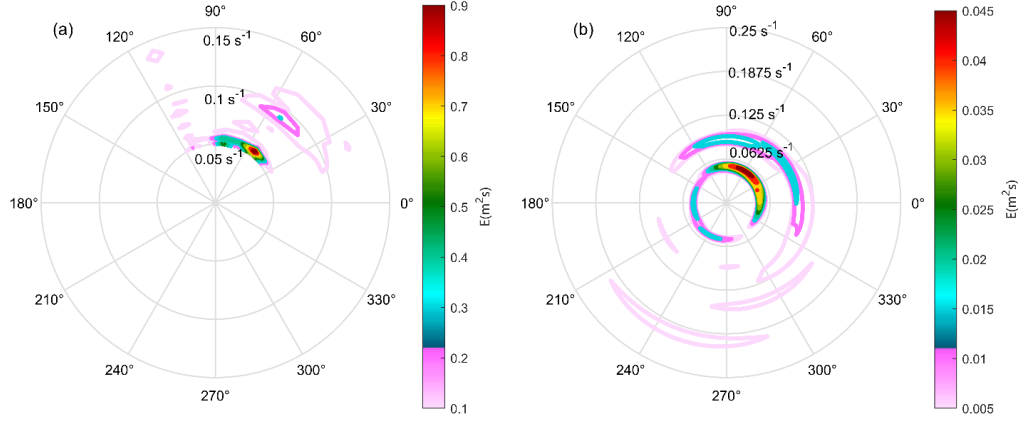

Figure 6. Two-dimensional wave spectra from (a) SWIM NRT data and (b) NDBC buoy data. These spectra correspond to the one-dimensional wave spectrum in Figure 5d.

Figures 5 and 6 show the distribution of swell energy with frequency and wave direction. To further analyze the influence of spherical spreading on swell decay, we calculated the spectral width on each route. This parameter is defined as follows (Longuet-Higgins, 1975):

$$\varepsilon^2 = 1 - \frac{m_2{}^2}{m_0 m_4}, \quad (5)$$

where m_0, m_2, and m_4 denote the zero-order moment, second-order moment, and fourth-order moment of the wave spectrum, respectively. The wave spectral moment is defined as follows:

$$m_n = \int_0^\infty \int_0^{2\Pi} \omega^n S(\omega, \varphi) \mathrm{d}\,\mathrm{d} \quad (6)$$

where $S(\omega, \varphi)$ represents the wave energy spectrum, which can be converted from the height spectrum $F(k, \varphi)$ as follows:

$$S(\omega, \varphi)\mathrm{d}\,\mathrm{d} = 2F(k, \varphi)\mathrm{k}\mathrm{d}\mathrm{k}\mathrm{d} \qquad (7)$$

and ω is the radian frequency. The value of the spectral width is between 0.2 and 0.9. The relationship between the spectral width and changes in wave parameters is shown in Figure 7. A larger spectral width leads to a higher decay rate of SWH and a higher growth rate of wavelength. The decay rate of SWH is defined as follows:

$$\mu_{\mathrm{decay}} = -\frac{\mathrm{SWH}_B - \mathrm{SWH}_C}{D_B - D_C}, \qquad (8)$$

where D is the distance to the source. The subscripts B and C stand for points B and C on the swell route, respectively. The correlation coefficient between the spectral width and μ_{decay} is 0.83, which demonstrates the significant influence of spherical spreading on swell attenuation. The growth rate of the swell wavelength is defined as follows:

$$\mu_{\mathrm{growth}} = \frac{L_B - L_C}{D_B - D_C} \qquad (9)$$

where L is the wavelength. The distribution of the points in Figure 7b indicates that the wavelength has a trend of increasing with distance, and μ_{growth} also increases with successive increases in spectral width.
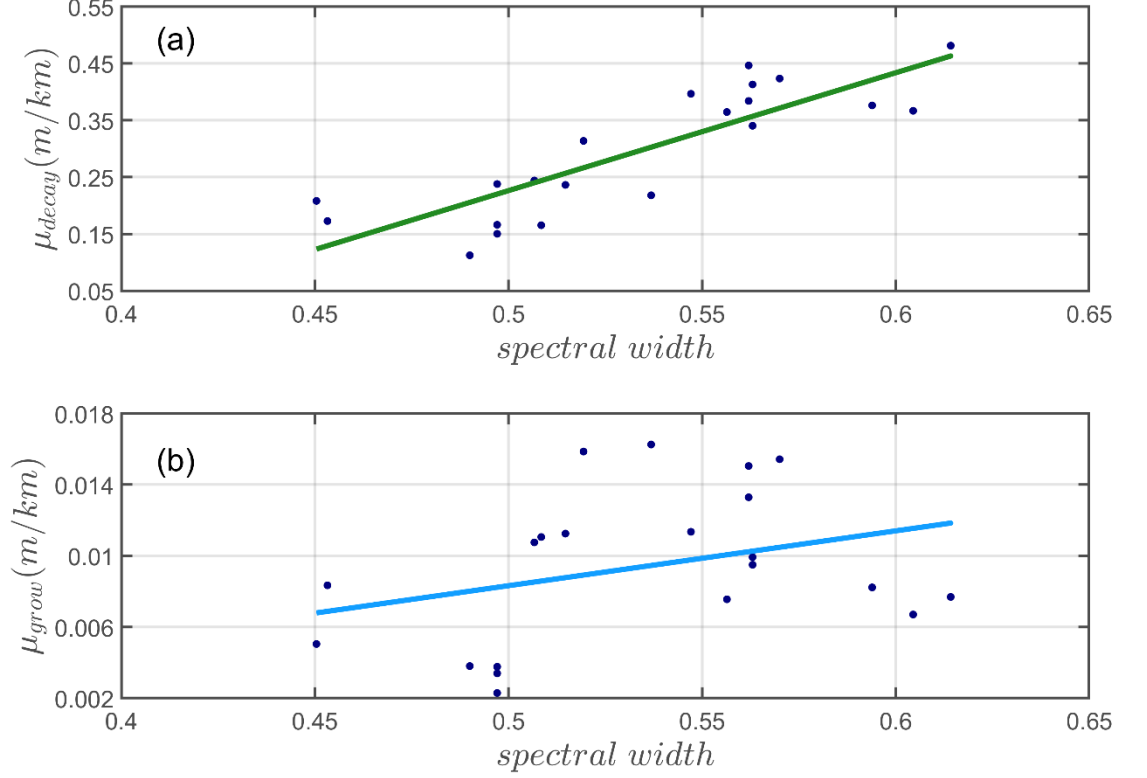
16

Figure 7. (a) Decay rate of SWH and (b) growth rate of wavelength with wave spectral width, and the linear fit shown.

4.3 Energy dissipation

When we trace the route of a wave group that propagates at a specific wave speed, we generally divide the energy decay along the propagation route into two main parts: spherical dispersion, which can lead to the deconcentration of wave energy; and dissipation, which can change the form of energy directly. The energy of swells might be transformed into turbulent kinetic energy via a non-breaking process (Babanin, 2012), or transferred to the atmospheric boundary layer during propagation (Ardhuin et al., 2009). In the present study, we used the observational data collected by the satellite and buoys to verify the theories proposed in previous studies, and explore the methods used to calculate the dissipation rates near the swell sources. To separate energy dissipation apart from energy decay caused by spherical spreading, we applied the two methods as described below.

4.3.1 Linear dissipation rate by point source assumption

17

The point source assumption is a generally accepted theory which states that energy is infinite at the source point from where all of the partitions of a swell field originate (Ardhuin et al., 2008; Snodgrass et al., 1966). If we use the linear model of this theory to characterize the energy decay of transoceanic swells, we have the following:

$$\mathrm{Es}_{\alpha_0} \alpha_0 \sin\alpha_0 = \mathrm{Es}_{\alpha_1} \alpha_1 \sin\alpha_1, \quad (10)$$

where α is the angular distance from the source and Es is the energy of the swell partition at different locations. Note that energy dissipation is ignored in this equation, and the difference between Es_{α_0} and Es_{α_1} is the energy decay caused by frequency dispersion and angular spreading between the two points. If we substitute the values at points C and B into Equation (10), we have the following:

$$\mathrm{Es}_{\alpha_B} \alpha_B \sin\alpha_B = \mathrm{Es}_{\alpha_C} \alpha_C \sin\alpha_C. \quad (11)$$

As the SWIM data have provided the SWH of each partition, we can easily calculate the swell energy at point C:

$$\mathrm{Es}_{\alpha_C} = \left(\frac{\mathrm{SWH}_{\alpha_C}}{4}\right)^2. \quad (12)$$

By adding Es_{α_C} to Equation (11) we obtain Es_{α_B}. As the NDBC buoy data provide only the

combined SWH of all wave partitions, we can use the watershed algorithm to partition the wave spectra to obtain the SWH of the swells (Hanson & Phillips, 2001). Figure 8 shows the energy decay from point C to point B without considering energy dissipation. The real and theoretical values of the swell energy at point B can be compared by assessing the distribution of green and blue points. Of the 21 cases, 14 show larger values of Es_{α_B} than the energy measured by NDBC, which signifies positive values for the dissipation rates.
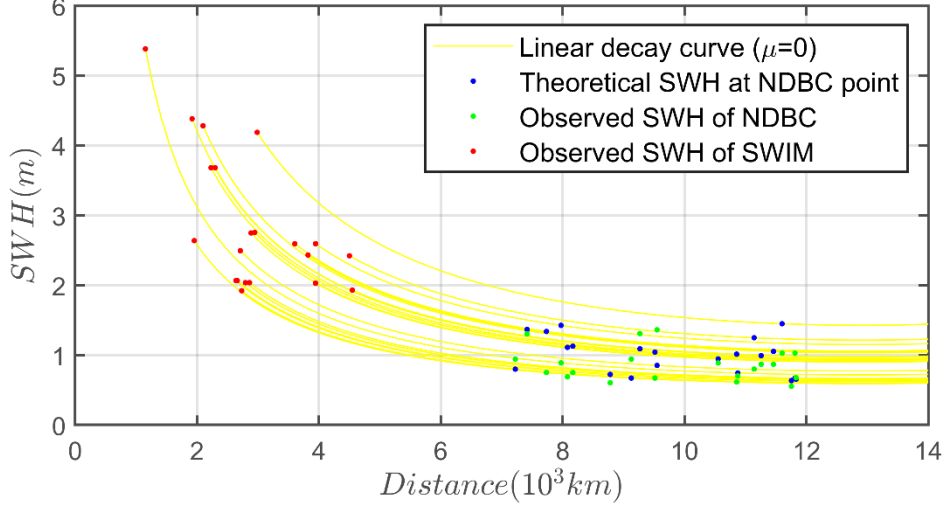
Figure 8. Linear decay (yellow curves) of swell SWH inferred from SWIM data (red points) and buoy data (blue points on the yellow curves are theoretical values, and green points are observed NDBC buoy data).

If we consider the influence of swell dissipation when referring to the point source model and assume a constant dissipation rate μ, then we have:

$$\mathrm{Es}_{\alpha_B}\alpha_B\sin\alpha_B = \mathrm{Es}_{\alpha_C}\alpha_C\sin\alpha_C e^{-\mathrm{R}(\alpha_B-\alpha_C)}, \quad (13)$$

where R is the radius of Earth. Note that Es_{α_B} in Equation (13) does not have the same meaning as in Equation (11); instead, it represents the observational energy at point B. The linear dissipation rate μ estimated from the 21 cases and using Equation (13) ranges from –1.4 to 2.4×10^{-7} m^{-1}, which is close to the range of –0.6 to 3.7×10^{-7} m^{-1} given by Ardhuin et al. (2009). The average value is 0.4×10^{-7} m^{-1}, and when the negative values are not considered, the average value increases to 1.0×10^{-7} m^{-1}.

4.3.2 Linear dissipation rate based on WW3 output

The point source model is applicable only if the distance from the source is greater than the source radius; therefore, we used it to calculate the dissipation rate from point C to point B (μ of R2). For R1 and R3, we used the data from the WW3 output (Test B) to obtain the energy loss caused by spherical dispersion. The model data include the value of SWH at points C and B from each swell route when ignoring the energy decay caused by swell dissipation and negative wind input during propagation. With these data, we can calculate the linear dissipation rate μ:

$$\mu = \frac{E_{\alpha}^{'} - E_{\alpha}}{R E_0}, \quad (14)$$

where $E_{\alpha}^{'}$ is the swell energy calculated with the WW3 output data, E_{α} is the real swell energy from the observations, E_0 is the energy of the swell source, and R is the earth radius. We checked the availability of the energy values obtained from the different datasets by doing some simple comparisons, and one of the cases was deleted from the dataset because the energy of the WW3 output at point C was greater than the source energy, which is unreasonable. Next, we calculated the dissipation rates of the other 20 cases of R1, which ranged from -3.6×10^{-8} to 2.1×10^{-7} m^{-1}, with an average value of 1.1×10^{-7} m^{-1}. The dissipation rates for the whole route (R3) ranged from 3.4×10^{-9} to 1.8×10^{-8} m^{-1}, with an average of 8.8×10^{-9} m^{-1}.

If we consider only the result obtained from the WW3 output data, we find that the dissipation rate of R1 clearly exceeds that of R3. We know that R1 is the section of the swell route that is closer to the source; consequently, the distance from the storm center may also be an important factor that influence the dissipation rates. We also conducted some comparisons between the cases, and Figure 9 shows that a negative correlation exists between the dissipation rates and the distance from the swell sources.
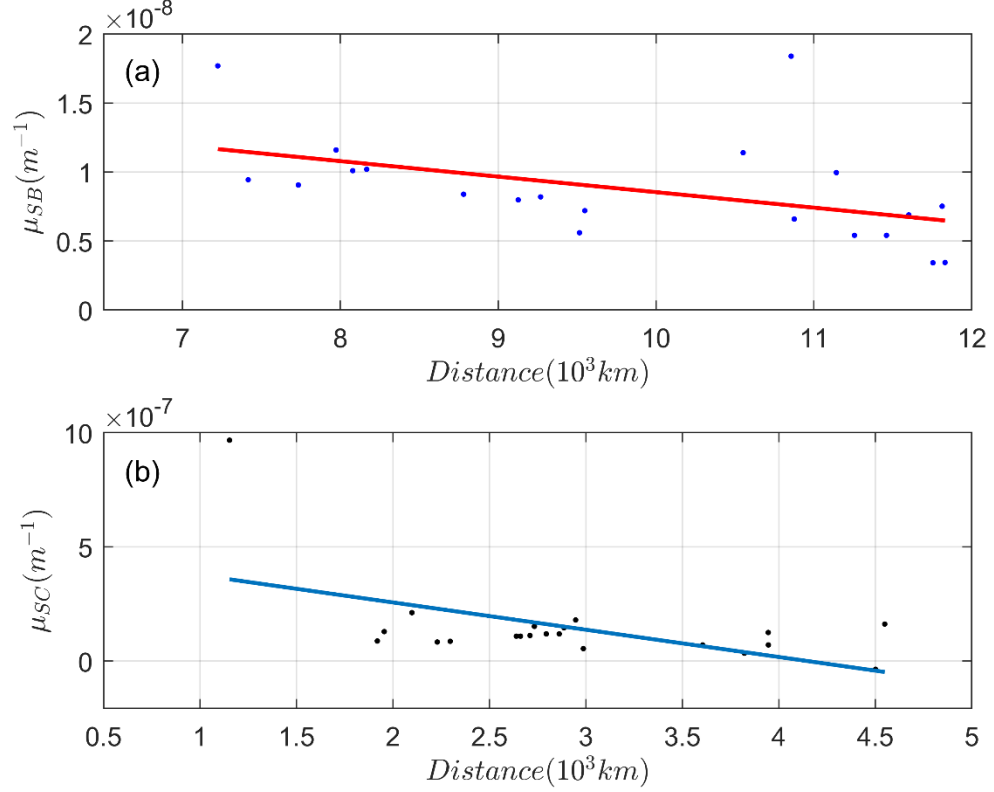
Figure 9. Swell dissipation rates with distance and the linear fit of (a) R3 and (b) R1.

Theoretically, the dissipation rates of R3 should be between the values of those of R1 and R2. However, our results show that R3 has the lowest dissipation rate, which is unreasonable. There are several possible reasons for this discrepancy. First, the error of the point source model can lead to deviation of results. Collard et al. (2009) reported that the swell energy calculated using the point source model deviates from the asymptotic values by less than 20% when the distance from the swell source is more than 4000 km, but most of the SWIM data of the present study are closer to the storm center, which may cause an increase in the errors. Second, the output data from the wave model can be a source of error. The run of the wave model covers the period from May to July, which means that the swell dissipation term and negative wind input term are neglected from the start of the model run, not from the time when the swells are generated. Thus, the WW3 output of SWH for the swell source is larger than the observational data, and this will further lead to a high value of SWH output at points C and B. The energy sink of swell dissipation is underestimated, and the dissipation rates obtained with this method are generally small.

21

4.3.3 Nonlinear dissipation rate

The linear dissipation rate can give the magnitude of swell dissipation, but it cannot explain the mechanism associated with the physical processes. We have mentioned above that several mechanisms have been proposed to interpret the process of swell dissipation. The relevant parameters here are not assumed to be constant along the whole route; instead, they are related to the state of the waves, and are the so-called nonlinear dissipation rates. The two important theories that have been applied to wave forecasts are the air–sea interaction theory proposed by Ardhuin et al. (2009) and the wave–turbulence interaction theory proposed by Babanin (2012).

Ardhuin et al. (2009) proposed that the wave orbital motion can lead to an energy flux from ocean to atmosphere, caused mainly by shear stress modulation. The dissipation of swells caused by this process can thus contribute to the generation of a wave-driven wind. The mechanism of dissipation is relevant to the transition of air-sea boundary layer from laminar to turbulent, which can be characterized using the Reynolds number ($\mathrm{Re} = 4u_{\mathrm{orb}}a_{\mathrm{orb}}/\nu$). When $\mathrm{Re} < 10^5$, viscosity plays an important role in dissipation. The nonlinear dissipation factor α_ν is given as follows:

$$\alpha_\nu = 2\frac{\rho_a 2\pi}{\rho_w c_g L}\sqrt{\frac{4}{T}}, \quad (15)$$

where ρ_a and ρ_w are the density of air and water, respectively, and the value of the air viscosity $=1.4\times10^{-5}$ m^2 s^{-1} (Dore, 1978). As $c_g = \frac{\mathrm{g}T}{4\pi}$ and $L = \frac{gT^2}{2\pi}$, α_ν is a function only of T. Here, we take the wave period at point C because it is located in the middle of every swell route and is more representative of the conditions along the whole route. For T_{SWIM} from 16.8 to 19.2 s, α_ν decreases from 8.9×10^{-9} to 5.6×10^{-9} m^{-1}.

When $\mathrm{Re} > 10^5$, the dissipation rate of swell over time is defined as follows:

$$\beta = C_g\mu = \frac{\rho_a 64\pi^2}{\rho_w gT^2}f_e u_{\mathrm{orb}}, \quad (16)$$

where f_e is a constant related to dissipation. By fitting the value of f_e to the observational data and the linear dissipation obtained from R2, we get a range of –0.017 to 0.034, which is comparable to the range of –0.015 to 0.03 given by Jiang et al. (2016). The mean value of f_e is 0.0055 and the standard deviation is 0.013.

The wave–turbulence interaction theory is another possible explanation for the dissipation of swells. The background turbulence on the swell routes and the turbulence directly induced by swell motion can consume the energy of swells and therefore lead to swell dissipation. Laboratory experiments have demonstrated

that when the wave-amplitude-based Reynolds Number (WRN $= u_{\mathrm{orb}}a_{\mathrm{orb}}/\nu$)
is larger than about 1300, wave orbital motion can induce turbulence inter-
mittently, and a fully turbulent state of wave motion needs a higher value of
WRN (Babanin, 2006; Dai et al., 2010). The volumetric dissipation rate $\varepsilon_{\mathrm{dis}}$ is
parameterized as follows:

$$\varepsilon_{\mathrm{dis}} = b_1 k u_{\mathrm{orb}}^3, \quad (17)$$

where k represents the wave number and u_{orb} is the wave orbital speed. As the
turbulence is found to be intermittent, the dissipation rate $\varepsilon_{\mathrm{dis}}$ can be influenced
by b_1, which is a parameter relevant to how long turbulence occurs during one
wave period.

Both of the above mechanisms are thought to be reasonable explanations for
swell dissipation. Young et al. (2013) found similarities in the formulas for the
two mechanisms and developed a new formula to show the relationship between
the two parameters b_1 and f_e:

$$b_1 = 24 f_e \rho_a / \rho_w. \quad (18)$$

Taking the value of f_e into Equation (18), we obtain b_1 values of –0.0005 to
0.001.

1. Conclusions

In this study, 25 swells recorded by NDBC buoys off the western coast of North
America were further connected with CFOSAT SWIM data and we confirmed
that they had originated in the Southern Ocean and then spread over long
distances before finally being observed by the buoys. These transoceanic swells
were related to four ocean storms that occurred between May and July 2019.
As the storms moved over the ocean, swells were radiated continuously.

Swells are attenuated slightly during propagation, owing mainly to frequency
dispersion, angular spreading, and non-breaking dissipation. To better under-
stand this process, we compared the wave spectra derived from the SWIM and
NDBC data. Swell decay is shown clearly by the decrease in energy density from
near the source to the more distant points. By calculating the value of the wave
spectral width, we found that a more dispersed distribution of energy can lead
to a higher rate of wavelength growth and energy decay, which demonstrates
the significant effect of spherical spreading.

To remove the effect of spherical spreading, we first used the point source model
before calculating the dissipation rates. In some cases, the dissipation rates were
negative, possibly due to instrumental error or environmental factors that we
did not consider, such as the strong winds or currents that can affect the energy

of swells. Using the linear decay model, the dissipation rate was found to fall within the range –1.4 to 2.4×10^{-7} m^{-1}, which is consistent with previous studies. The present study is the first to use WW3 output data to help calculate the swell dissipation rates. The model data were compared with observational data to calculate the linear dissipation rates of swells from swell sources. The dissipation rates decreased with increasing distance from the storm center. However, the dissipation rates from different stages of swell propagation were calculated using the above two different methods, which yielded contrasting results due to systematic errors. We may solve this problem in the future by collecting more data and using a more accurate starting time for each swell route.

The non-linear dissipation rate is related to different physical mechanisms depending on the Reynolds number. When $\text{Re} < 10^5$, the dissipation of swells is thought to be caused mainly by viscosity, and the dissipation rate is a function only of wave period. When the value of Re is larger, the effect of turbulence becomes more important. When we considered the interaction of swells with the background turbulence in the ocean or the turbulence caused directly by swell motion, the coefficient b_1 was found to vary between –0.0005 and 0.001. Similarly, when we considered the effect of turbulence at the air–sea boundary layer, the coefficient f_e varied between –0.017 and 0.034.

We used CFOSAT SWIM data for the first time to perform swell tracing and analyze the process of swell decay across the ocean. The wave spectrum data obtained from SWIM and the NDBC buoys provided us with a more intuitive way to observe the decay of energy. With reference to previous theories, we calculated the linear and non-linear dissipation rates. The ranges of the dissipation coefficients were similar to those reported in previous studies, but the accuracy of the results will require further improvement in a future study using larger datasets and updated versions of the data. In addition, if the change in wave spectral structure for each swell route can be analyzed in combination with environmental factors, it might be possible to develop a better understanding of swell decay and the underlying mechanisms.

Acknowledgments

Data Availability Statement

The data directly used in this study are available in https://figshare.com/art icles/dataset/Tracing_the_decaying_swell_across_Pacific_with_CFOSA T_SWIM_data/19127555. The buoy data are taken from National Data Buoy Center (https://www.ndbc.noaa.gov/). The Surface Waves Investigation and Monitoring (SWIM) data are available in ftp://ftp-access.aviso.altimetry.fr/. The ERA5 reanalysis data with 0.5°×0.5° horizontal resolution are taken from the European Centre for Medium-Range Weather Forecasts (https://www.ec

mwf.int/en/forecasts/datasets/reanalysis-datasets/era5). And the WW3 output data are available in https://figshare.com/articles/dataset/Tracing_t he_decaying_swell_across_Pacific_with_CFOSAT_SWIM_data/19127555.

Reference

Alves, J.-H. G. (2006), Numerical modeling of ocean swell contributions to the global wind-wave climate, *Ocean Modelling*, *11*(1-2), 98-122. http://doi.org/10 .1016/j.ocemod.2004.11.007

Andrade, C. A., Thomas, Y. F., Lerma, A. N., Durand, P., & Anselme, B. (2013), Coastal flooding hazard related to swell events in Cartagena de Indias, Colombia, *Journal of Coastal Research*, *29*(5), 1126-1136. http://doi.org/10.2 112/JCOASTRES-D-12-00028.1

Ardhuin, F., Chapron, B., & Collard, F. (2009), Observation of swell dissipation across oceans, *Geophysical Research Letters*, *36*(6). http://doi.org/10.1029/20 08GL037030

Babanin, A. V. (2006), On a wave-induced turbulence and a wave-mixed upper ocean layer, *Geophysical Research Letters*, *33*(20). http://doi.org/10.1029/20 06GL027308

Babanin, A. V. (2012), Swell attenuation due to wave-induced turbulence, paper presented at International Conference on Offshore Mechanics and Arctic Engineering, American Society of Mechanical Engineers. http://doi.org/10.111 5/OMAE2012-83706

Badulin, S. I., & Zakharov, V. E. (2017), Ocean swell within the kinetic equation for water waves, *Nonlinear Processes in Geophysics*, *24*(2), 237-253. http://doi. org/10.5194/npg-24-237-2017

Chen, G., Chapron, B., Ezraty, R., & Vandemark, D. (2002), A global view of swell and wind sea climate in the ocean by satellite altimeter and scatterometer, *Journal of Atmospheric and Oceanic Technology*, *19*(11), 1849-1859. http://do i.org/10.1175/1520-0426(2002)019%3c1849:AGVOSA%3e2.0.CO;2

Collard, F., Ardhuin, F., & Chapron, B. (2009), Monitoring and analysis of ocean swell fields from space: New methods for routine observations, *Journal of Geophysical Research: Oceans*, *114*(C7), C07023. http://doi.org/10.1029/20 08JC005215

Dai, D., Qiao, F., Sulisz, W., Han, L., & Babanin, A. (2010), An experiment on the nonbreaking surface-wave-induced vertical mixing, *Journal of Physical Oceanography*, *40*(9), 2180-2188. http://doi.org/10.1175/2010JPO4378.1

Dore, B. (1978), Some effects of the air-water interface on gravity waves, *Geophysical & Astrophysical Fluid Dynamics*, *10*(1), 215-230. http://doi.org/10.1 080/03091927808242638

Drennan, W. M., Graber, H. C., & Donelan, M. A. (1999), Evidence for the Effects of Swell and Unsteady Winds on Marine Wind Stress, *Journal of Physical*

Oceanography, *29*(8), 1853-1864. http://doi.org/10.1175/1520-0485(1999)029 %3c1853:Efteos%3e2.0.Co;2

Hamilton, G. D. (1992), Measurement of long-period, low-amplitude swell in the western North Atlantic Ocean, *Journal of Atmospheric and Oceanic Technology*, *9*(5), 645-658. http://doi.org/10.1175/1520-0426(1992)009%3c0645:MOLPLA %3e2.0.CO;2

Hanson, J. L., & Phillips, O. M. (2001), Automated Analysis of Ocean Surface Directional Wave Spectra, *Journal of Atmospheric and Oceanic Technology*, *18*(2), 277-293. http://doi.org/10.1175/1520-0426(2001)018%3c0277: Aaoosd%3e2.0.Co;2

Hauser, D., et al. (2021), New Observations From the SWIM Radar On-Board CFOSAT: Instrument Validation and Ocean Wave Measurement Assessment, IEEE Transactions on Geoscience and Remote Sensing, 59, 5-26. http://doi.or g/10.1109/tgrs.2020.2994372

Hersbach, H., et al. (2020), The ERA5 global reanalysis, Quarterly Journal of the Royal Meteorological Society, 146(730), 1999-2049. http://doi.org/https: //doi.org/10.1002/qj.3803

Hwang, P. A. (2008), Observations of swell influence on ocean surface roughness, *Journal of Geophysical Research: Oceans*, *113*(C12). http://doi.org/10.1029/ 2008jc005075

Jiang, H., Stopa, J. E., Wang, H., Husson, R., Mouche, A., Chapron, B., & Chen, G. (2016), Tracking the attenuation and nonbreaking dissipation of swells using altimeters, *Journal of Geophysical Research: Oceans*, *121*(2), 1446-1458. http://doi.org/10.1002/2015JC011536

Krogstad, H. E. (1992), A simple derivation of Hasselmann's nonlinear ocean-synthetic aperture radar transform, Journal of Geophysical Research: Oceans, 97(C2), 2421-2425. http://doi.org/https://doi.org/10.1029/91JC03010

Kudryavtsev, V. N., & Makin, V. K. (2004), Impact of Swell on the Marine Atmospheric Boundary Layer, *Journal of Physical Oceanography*, *34*(4), 934-949. http://doi.org/10.1175/1520-0485(2004)034%3c0934:Iosotm%3e2.0.Co;2

Li, X.-M. (2016), A new insight from space into swell propagation and crossing in the global oceans, *Geophysical Research Letters*, *43*(10), 5202-5209. http: //doi.org/10.1002/2016GL068702

Liu, Q., Rogers, W. E., Babanin, A. V., Young, I. R., Romero, L., Zieger, S., Qiao, F., & Guan, C. (2019), Observation-Based Source Terms in the Third-Generation Wave Model WAVEWATCH III: Updates and Verification, Journal of Physical Oceanography, 49(2), 489-517. http://doi.org/10.1175/jpo-d-18-0137.1

Liu, Q., et al. (2021), Global Wave Hindcasts Using the Observation-Based Source Terms: Description and Validation, *Journal of Advances in Modeling*

Earth Systems, *13*(8), e2021MS002493. http://doi.org/https://doi.org/10.102 9/2021MS002493

Longuet-Higgins, M. S. (1975), On the joint distribution of the periods and amplitudes of sea waves, Journal of Geophysical Research (1896-1977), 80(18), 2688-2694. http://doi.org/https://doi.org/10.1029/JC080i018p02688

Munk, W. H., Miller, G., Snodgrass, F., & Barber, N. F. (1963), Directional recording of swell from distant storms, *Philosophical Transactions of the Royal Society of London. Series A, Mathematical and Physical Sciences*, *255*(1062), 505-584. http://doi.org/10.1098/rsta.2013.0039

Remya, P., Vishnu, S., Praveen Kumar, B., Balakrishnan Nair, T., & Rohith, B. (2016), Teleconnection between the North Indian Ocean high swell events and meteorological conditions over the Southern Indian Ocean, *Journal of Geophysical Research: Oceans*, *121*(10), 7476-7494. http://doi.org/10.1002/2016JC01 1723

Rogers, W. E., & Linzell, R. S. (2018), The IRI Grid System for Use with WAVEWATCH III®, *NRL Memorandum Report*, 7320-7318.

Semedo, A., Sušelj, K., Rutgersson, A., & Sterl, A. (2011), A Global View on the Wind Sea and Swell Climate and Variability from ERA-40, *Journal of Climate*, *24*(5), 1461-1479. http://doi.org/10.1175/2010jcli3718.1

Snodgrass, F., Hasselmann, K., Miller, G., Munk, W. H., & Powers, W. (1966), Propagation of ocean swell across the Pacific, *Philosophical Transactions of the Royal Society of London. Series A, Mathematical and Physical Sciences*, *259*(1103), 431-497. http://doi.org/10.1098/rsta.1966.0022

The WAVEWATCH III Development Group (WW3DG) (2019), User manual and system documentation of WAVEWATCH III TM version 6.07, *NOAA/NWS/NCEP/MMAB Technical Note 333*, 465.

Wang, X., Jiang, H., Chen, G., & Yu, F. (2016), Identifying storm-induced wave origins using SAR wave mode data, *Science China Earth Sciences*, *59*(10), 1971-1980. http://doi.org/s11430-015-5478-3

Young, I. R., Babanin, A. V., & Zieger, S. (2013), The decay rate of ocean swell observed by altimeter, *Journal of physical oceanography*, *43*(11), 2322-2333. http://doi.org/10.1175/JPO-D-13-083.1

Zhang, Z., & Li, X.-M. (2017), Global ship accidents and ocean swell-related sea states, *Natural Hazards & Earth System Sciences*, *17*(11). http://doi.org/ 10.5194/nhess-17-2041-2017

Zheng, C., Li, C., & Pan, J. (2018), Propagation route and speed of swell in the Indian Ocean, *Journal of Geophysical Research: Oceans*, *123*(1), 8-21. http://doi.org/10.1002/2016JC012585

Zheng, K., Sun, J., Guan, C., & Shao, W. (2016), Analysis of the global swell and wind sea energy distribution using WAVEWATCH III, *Advances in Meteorology*,

2016. http://doi.org/10.1155/2016/8419580

Zieger, S., Babanin, A. V., Rogers, W. E., & Young, I. R. (2015), Observation-based source terms in the third-generation wave model WAVEWATCH, *Ocean Modelling*, *96*, 2-25. http://doi.org/10.1016/j.ocemod.2015.07.014